

Emergent impervious band crossing in the bulk in topological nodal line semimetal ZrAs₂

A. S. Wadge^{1*}, K. Zborecki^{3†}, B. J. Kowalski², D. Jastrzebski^{1,2,5}, P. K. Tanwar¹, P. Iwanowski², R. Diduszko², A. Moosarikandy¹, M. Rosmus⁴, N. Olszowska⁴ and A. Wisniewski^{1,2}

¹ *International Research Centre MagTop, Institute of Physics, Polish Academy of Sciences, Aleja Lotnikow 32/46, PL-02668 Warsaw, Poland*

² *Institute of Physics, Polish Academy of Sciences, Aleja Lotnikow 32/46, PL-02668 Warsaw, Poland*

³ *Faculty of Physics, Warsaw University of Technology, Koszykowa 75, Warsaw, 00-662, Poland*

⁴ *National Synchrotron Radiation Centre SOLARIS, Jagiellonian University, Czerwone Maki 98, PL-30392 Cracow, Poland*

⁵ *Faculty of Chemistry, Warsaw University of Technology, Noakowskiego 3, 00-664 Warsaw, Poland*

[*wadge@magtop.ifpan.edu.pl](mailto:wadge@magtop.ifpan.edu.pl)

[†Krzysztof.Zborecki@pw.edu.pl](mailto:Krzysztof.Zborecki@pw.edu.pl)

ABSTRACT:

Topological nodal line semimetals (TSMs) represent a unique class of materials with intriguing electronic structures and rich of symmetries, hosting electronic states with non-trivial topological properties. Among these, ZrAs₂ stands out, characterized by its nodal lines forming continuous loops in momentum space, governed by non-symmorphic symmetries. This study integrates angle-resolved photoemission spectroscopy (ARPES) with density functional theory (DFT) calculations to explore the electronic states of ZrAs₂. In ARPES scans, we observed a distinctive nodal loop structure observed at lower excitation energies of 30 and 50 eV. Our results, supported by calculations based on DFT, unveil symmetry-enforced Dirac-like band crossings anchored at specific points in the Brillouin zone, with particular emphasis on the S point. Surface bands and bulk states near the crossing are elucidated through slab calculations, corroborating experimental findings. DFT calculations also show the existence of several spin-orbit coupling (SOC) resilient semi-Dirac crossings pinned at Z point. This comprehensive investigation sheds light on the intricate electronic behaviors of ZrAs₂ with the involved symmetries, important for fundamental understanding of topological nodal line semimetals.

I. INTRODUCTION

Topological semimetals (TSMs) represent a novel class of materials in condensed matter physics, distinguished by their unique electronic structures and the intricate role of symmetries. These materials are known for hosting electronic states that exhibit non-trivial topological properties [1-5]. In their electronic structure, the bands meet at certain isolated points or lines in momentum space, giving rise to anomalous contribution to the physical properties [6,7]. Angle-resolved photoemission spectroscopy (ARPES) plays a pivotal role in this research field by providing direct insights into the electronic band structures of the materials, enabling us to observe and characterize symmetry-protected surface states [8-11].

Topological nodal line semimetal is one of the types of TSMs where the conduction and valence bands intersect not at discrete points, but along continuous loop in the momentum space, forming one dimensional 'nodal line'. These materials are mostly rich with symmetries such as non-symmorphic, inversion and time-reversal ones. Among them non-symmorphic symmetry is sparsely seen in the semimetal, which involves a partial lattice shift combined with either mirror reflection (forming a glide plane) or a rotation (creating a screw axis). This leads to band-folding and crossings at the edges of the Brillouin zone (BZ). They are known as essential band crossings and are resilient to the effects of spin-orbit coupling (SOC) as long as the non-symmorphic symmetry is maintained [12-14]. Non-symmorphic symmetry also preserves so called semi-Dirac band crossings, exhibiting a close resemblance to the massless fermions in one direction. However, it behaves as a zero-gap semiconductor in [010] direction, displaying the finite effective mass. These distinct features contribute to the unique transport properties of the material. These crossings are protected from the effect of SOC [7]. While there are numerous materials which show the gap opening due to SOC, only few materials exhibit non-symmorphic symmetry-protected Dirac-like crossings [15-18].

In 2016, Schoop et al. conducted a comprehensive theory and ARPES study on ZrSiS, revealing a Dirac cone protected by non-symmorphic symmetry and the presence of three-dimensional Dirac lines [19]. In the same year, Takane et al. unearthed a Dirac node arc in the topological line node semimetal HfSiS, a finding that emphasized the intricate nature and promising capabilities of HfSiS [20]. Further advancements by Sims et al. revealed surface states in HfP₂ which vary depending on the material's termination [21]. Later, Zhou et al. provided theoretical insights into non-symmorphic symmetry and butterfly-like nodal lines in ZrAs₂, a study that was critical in understanding the material's high-symmetry path properties [8]. Bannies et al. enhanced our knowledge through ARPES spectra studies on ZrP₂ in 2021 [22]. Simultaneously, in the same year, Hao et al. identified multiple Dirac nodal lines in TaNiTe₅, further broadening our perspective [23] and the very recent contribution to the field by Wu et al. who identified non-symmorphic symmetry-protected band crossings in the square net metal PtPb₄ [24]. Also Mohanta, Meng et al. and Fakherdine et al. theoretically showed the non-symmorphic symmetry protected semi-Dirac crossings fixed at the boundary of Brillouin zone [7, 25, 26].

Referring to the previous studies, this paper introduces ARPES investigation of a nodal line semimetal ZrAs_2 supported by DFT calculations. It shows non-symmorphic symmetry protected Dirac like band crossing at the boundary of the Brillouin zone.

II. EXPERIMENTAL DETAILS

i. Single crystal growth and structural characterization

Single crystals of ZrAs_2 were grown using the two-stage chemical vapor transport (CVT) method, as shown in Figure 1. Initially, polycrystalline ZrAs_2 was synthesized through the direct reaction of Zr sponge (Koch-Light Laboratories Ltd, 99.8%) and As (PPM Pure Metals, 99.999995%) in an evacuated quartz ampoule. The ampoule was maintained for 7 days at 800 °C, with the other end kept at 460 °C to safely reduce the internal pressure. The resulting polycrystalline ZrAs_2 was pressed into pellets, loaded into a quartz tube with iodine (POCH, 99.8%, 10 mg/cm³ of ampoule volume) as transport agent and sealed under vacuum. This assembly was then placed in a furnace with a temperature gradient of 700 °C (source zone) and 800 °C (crystallization zone) for 21 days. Afterward, the furnace was turned off and allowed to cool down to room temperature.

Crystal structure and crystallographic quality of grown ZrAs_2 were verified by x-ray powder diffraction using a Rigaku SmartLab 3kW diffractometer equipped with a tube having Cu anode, and operating with $U = 40$ kV and $I = 30$ mA. The characteristic peak positions were identified, as shown in Fig. 1(c), based on the data from International Centre for Diffraction Data (ICDD), Powder Diffraction File PDF-4+2023 RDB database.

For the quantitative chemical analysis of ZrAs_2 , Energy Dispersive X-ray Spectroscopy (EDX) was employed using a QUANTAX 400 Bruker system coupled with a Zeiss Auriga field-emission (Schottky-type) scanning electron microscope. The EDX measurements were conducted at 15-kV incident energy. The sample was prepared by sticking the crystals of ZrAs_2 on the carbon tape. Oriented samples were utilized, and the results confirmed the stoichiometric composition of ZrAs_2 , with an atomic ratio of 1:2, within the experimental error margin.

ii. ARPES setup

Our experiment was conducted using the URANOS beamline at the National Synchrotron Radiation Centre SOLARIS in Krakow, Poland. The radiation source for our measurements was a quasiperiodic elliptically polarizing APPLE II type undulator, emitting photons in the energy range of 8–170 eV. The facility was outfitted with the SCIENTA OMICRON DA30L photoelectron spectrometer with energy and angular resolutions of 1.8 meV and 0.1°, having deflectors that enable wide-angle band structure measurements without the need to change the position of the sample. This setup enabled us to perform precise band-mapping across the entire Brillouin Zone (BZ). ARPES spectra were obtained from single crystals that were freshly cleaved in situ within an ultra-high vacuum (UHV) ($\sim 3.7 \times 10^{-11}$ torr) environment to obtain (0 0 1) surface, using excitation energies of 30 eV and 100 eV. During these measurements, the samples were consistently maintained at a temperature of 80 K.

The analysis of the gathered ARPES data was conducted using IGOR PRO software and Python scripts.

III. DFT CALCULATION DETAILS

All the calculations were performed within density functional theory (DFT) as implemented in the VASP Package [27-30] with Projector augmented wave pseudopotentials (PAW) [31, 32] and PBE (GGA) functional [33]. For the sampling of the Brillouin zone, a dense $8 \times 8 \times 8$ grid was used, while the plane wave energy cutoff was set to 520 eV. All the structures were optimized until the force exerted on each ion was smaller than 10^{-5} eV/Å. 3D plots of Fermi surface were made with use of the XCrysDen code [34]. For further evaluation of the DFT results, the tight binding (TB) model was prepared with use of the Wannier90 code [36]. This model was used to calculate surface states of the slab structure with use of the Wannier Tools package [37].

IV. RESULTS AND DISCUSSIONS

The CVT process produced needle-like single crystals of ZrAs_2 of length 5-6 mm (see Figure 1(b)). X-ray diffraction analysis showed that ZrAs_2 crystallizes in an orthorhombic crystal structure with space group number 62 (pnma, D_{2h}). It is centrosymmetric in nature with the refined lattice parameters $a = 6.80163(10)$ Å, $b = 3.68891(5)$ Å, $c = 9.03058(13)$ Å. ZrAs_2 has a non-magnetic ground state and it has non-symmorphic symmetry [8] with stoichiometric ratio of Zr:As as 1:2 (see suppl. Figure 1).

The X-ray diffraction data confirm the single crystalline phase and are consistent with previous studies [37, 38]. The calculated lattice constants obtained in relaxation process are within typical DFT deviation from the experimental values. In crystal structure of ZrAs_2 , the Zr ion (blue) is surrounded by nine As ions (tan). Additionally, the crystal has a horizontal and vertical glide planes as shown in Figure 2(a). In the Brillouin zone, (001) surface projection of 3D Brillouin zone is plotted with high symmetry points with $\bar{\Gamma}$ at the centre and 3D visualization $E(k_x, k_y)$ of bands depicted in Figure 2 (b and c), respectively.

The calculated plots in Figure 2 (d and e) along $\bar{X}-\bar{\Gamma}-\bar{Z}$ demonstrate the bulk band structure without and with SOC, respectively. The inclusion of SOC led to the gapping out of the nodal lines, creating a gap of approximately 15-20 meV. These plots are consistent with the previously reported theoretical band structure calculations [22]. The calculated Fermi surface for (001) plane of ZrAs_2 was shown in Figure 2(f) presenting electron and hole pockets. To get a more details, we have plotted the band structure using DFT calculations with SOC along high symmetry path as illustrated in the Figure 3 (a). It shows three types of band crossings indicated by different colors of dotted rectangles. The accidental band crossings (ABC) open the gap due to SOC (blue), whereas symmetry-enforced band crossings (SEBC) (purple) and semi-Dirac band crossings (yellow) are resilient to SOC and mainly protected by non-symmorphic symmetry. In Figure 3 (a), three significant bands are shown with red, blue and green colors. The red and blue color bands are related to the hole and electron pockets, respectively. The bands close to the Fermi level on path $\bar{\Gamma}-\bar{X}$ is a mixture of

p and d states, so it cannot be assigned to particular ions (Suppl. Figure 2). Figure 3 (b) displays the 3D Brillouin zone with the electron (blue) and hole (red) Fermi pockets. Unlike ZrP_2 , the third pocket with lowest energy is not present in ZrAs_2 [22].

The core-level spectra were taken prior to ARPES measurements in order to check the composition and they showed the significant peaks of Zr $3d_{3/2}$ (181.1 eV), Zr $3d_{5/2}$ (178.8 eV), Zr $4p_{1/2}$ (28.5 eV) as well as As $3s$ (204.7 eV), As $3p_{1/2}$ (146.2 eV), As $3p_{3/2}$ (141.2 eV), As $3d_{3/2}$ (41.7 eV), As $3p_{3/2}$ (41.7 eV) which are in good agreement with the binding energy database (see Figure 4(a)) [37]. The core-level spectrum shows more significant arsenic peaks which can manifest that the cleaved surface is As terminated. These peaks confirm the composition of Zr and As with no foreign quantity in the crystals. Later, the ARPES spectra were measured at excitation energies of 30 eV and 100 eV on freshly cleaved sample. Figure 4 (b and c) shows the 3D visualization of the Fermi surfaces at 30 and 100 eV, respectively. A distinctive nodal loop emerging within the $k_x = 0$ plane, positioned slightly below the Fermi level was obtained at low-energy excitation 30 and 50 eV whereas it is absent in the ARPES spectra at 100 eV (Suppl. Figure 4). The robustness of this nodal loop against gap formation is ensured by the existence of the glide planes shown within the crystal structure even though there is minor gap opening (approx. 15 meV) due to SOC. The constant energy contour at 30 eV with different binding energies showed the evolution from Fermi surface up to binding energy $EB = -1.06$ eV, which can be seen on Figures 5(a-d) at different EB. The cut along $\bar{X} - \bar{\Gamma} - \bar{X}$ shows the nodal lines surface states near the $\bar{\Gamma}$ point (see Figure 5 (f)) and the cut along $\bar{S} - \bar{Y} - \bar{S}$ was also shown. The consistency between both cross-sectional cuts and the DFT calculations showcased in Figures 5 (e) and (h), respectively is notable.

Along $\bar{X} - \bar{\Gamma} - \bar{X}$, the surface states are partially hybridized whereas within the projected bulk Fermi surface, there is envelopment by distinct surface states and along $\bar{S} - \bar{Y} - \bar{S}$ the surface states are clearly visible. Slab calculations shown in the Suppl. Figure 3 show good agreement with ARPES results. In Figure 6, we have shown a comparison of 2D Fermi surface and of iso-energetic surfaces for different binding energies obtained at corresponding binding energies from slab calculations. They are in excellent agreement with each other. The theoretical Fermi surfaces were obtained for the semi-infinite slab with orientation (001). To see the evolution of the Fermi surfaces the four energies have been chosen: Fermi surface ($E = E_F$), $E = -1.72$ eV and two intermediate values ($E = -0.5$ eV and $E = -1.0$ eV). For $E = E_F$, the electron and hole pockets (cf. Figure 3b) can be clearly visible. Lowering the energy, the hole pocket shrinks, while electron pocket becoming more robust. For $E = -1.72$ eV in the vicinity of the S point (Figure 6h) one can observe the pronounced signatures of the Dirac crossings. For completeness, in Suppl. Figure 5 one can see the butterfly shaped Fermi surfaces for $E = E_F$, projected on the (100) and (010) planes, on which both electron (e) and hole (h) pockets are visible.

Another important finding of our work is symmetry enforced band crossings in the bulk. Non-symmorphic symmetry alone ensures only the existence of band crossing in the band dispersion, yet it does not determine the specific location of this degenerate point in

momentum space. However, presence of inversion symmetry anchored the band crossing either at the $\bar{\Gamma}$ point or along the boundary of the Brillouin Zone (BZ) [14]. ZrAs_2 shows an orthorhombic crystal structure with non-symmorphic symmetry and inversion symmetry [8]. DFT calculated bulk band dispersions (shown in Figure 7 (a and b)) displays that the band crossing which is fixed at \bar{S} point has four-fold degeneracy in the absence of SOC. Since non-symmorphic symmetry is robust against SOC, there are two-fold degenerated crossings at S point (Figure 7(b)). The slab calculations in Figure 8 (a) show that surface and bulk bands hybridized near this crossing with dominating bulk states. The results display slab calculations, showcasing the projection of bands onto an iso-energetic surface computed at -1.72 eV whereas Figure 8 (b) depicts the comparison between calculated bands (depicted as green dotted lines) and experimental bands obtained through ARPES. This comparison reveals potential Dirac crossings at \bar{S} points. Additionally, the presentation includes multiple slices along the $\bar{X} - \bar{S} - \bar{X}$ direction, offering a visual representation of the band evolution across $\bar{S} - \bar{Y} - \bar{S}$.

V. CONCLUSIONS

We observed a 3D band structure of ZrAs_2 with electron and hole pockets that influence the material's electronic properties. The band structure calculated by DFT, including spin-orbit coupling, revealed three types of band crossings: accidental band crossings (ABC), symmetry-enforced band crossings (SEBC), and semi-Dirac crossings (SDBC). SEBC and SDBC were primarily protected by non-symmorphic symmetry within the crystal. Analysis of ARPES data obtained from in-situ cleaving at the (001) plane showed that for lower excitation energies nodal lines manifested themselves at $\bar{\Gamma}$ point, whereas they were absent at 100 eV, consistent with DFT and slab calculations. Notably, SEBC was observed at $E_B = -1.72$ eV (S point), indicating dominant bulk states. However, due to cleaving at the (001) plane, we were unable to observe semi-Dirac crossings, which are anticipated to be observed at the (010) plane.

ACKNOWLEDGEMENTS

We are grateful to B. Turowski for his invaluable assistance with ARPES cube data procedures, and to K. Cieslak for her support at the beamline. We thank C. Autieri, R. Bacewicz, S. Jatrębski, and W. Paszkowicz for their insightful discussions. This research was made possible through the support of the Foundation for Polish Science, facilitated by the IRA Programme and co-financed by the European Union within the framework of the Smart Growth Operational Programme (Grant No. MAB/2017/1). We acknowledge with appreciation the SOLARIS Centre for providing access to Beamline UARPES, where the crucial ARPES measurements were conducted. Additionally, we express our appreciation to Poland's high-performance infrastructure PLGrid, operated by Cyfronet AGH, for providing computational facilities and support under computational grant no plgnanotrans10.

REFERENCES

- [1] C. Xu, J. Chen, G. X. Zhi, Y. Li, J. Dai, and C. Cao, *Electronic Structures of Transition Metal Dipnictides $X\text{Pn}_2$ ($X=\text{Ta}, \text{Nb}$; $\text{Pn}=\text{P}, \text{As}, \text{Sb}$)*, Phys. Rev. B **93**, 1 (2016).
- [2] Y. Shao, Z. Sun, Y. Wang, C. Xu, R. Sankar, A. J. Breindel, C. Cao, M. M. Fogler, A. J. Millis, F. Chou, Z. Li, T. Timusk, M. Brian Maple, and D. N. Basov, *Optical Signatures of Dirac Nodal Lines in NbAs_2* , Proc. Natl. Acad. Sci. U. S. A. **116**, 1168 (2019)
- [3] J. Chen, Y. K. Li, J. Dai, and C. Cao, *Electronic Structure and Topological Properties of Centrosymmetric $\text{MoAs}_2/\text{WAs}_2$ from First Principles*, Sci. Rep. **7**, 10491 (2017).
- [4] B. Wang, B. Singh, B. Ghosh, W. C. Chiu, M. M. Hosen, Q. Zhang, L. Ying, M. Neupane, A. Agarwal, H. Lin, and A. Bansil, *Topological Crystalline Insulator State with Type-II Dirac Fermions in Transition Metal Dipnictides*, Phys. Rev. B **100**, 1 (2019).
- [5] A. J. H. Jones and R. Muzzio, *Electronic Properties of TaAs_2 Topological Semimetal Investigated by Transport and ARPES*, J. Phys. Condens. Matter **34**, 125601 (2022).
- [6] S. Li, Y. Liu, S. S. Wang, Z. M. Yu, S. Guan, X. L. Sheng, Y. Yao, and S. A. Yang, *Nonsymmorphic-Symmetry-Protected Hourglass Dirac Loop, Nodal Line, and Dirac Point in Bulk and Monolayer $X_3\text{SiTe}_6$ ($X = \text{Ta}, \text{Nb}$)*, Phys. Rev. B **97**, 045131 (2018).
- [7] A. Fakhredine, R. M. Sattigeri, G. Cuono, and C. Autieri, *Interplay between Altermagnetism and Nonsymmorphic Symmetries Generating Large Anomalous Hall Conductivity by Semi-Dirac Points Induced Anticrossings*, Phys. Rev. B **108**, 115138 (2023).
- [8] X. Zhou, C. H. Hsu, H. Aramberri, M. Iraola, C. Y. Huang, J. L. Mañes, M. G. Vergniory, H. Lin, and N. Kioussis, *Novel Family of Topological Semimetals with Butterflylike Nodal Lines*, Phys. Rev. B **104**, 125135 (2021).
- [9] H. Yang, A. Liang, C. Chen, C. Zhang, N. B. M. Schroeter, and Y. Chen, *Visualizing Electronic Structures of Quantum Materials by Angle-Resolved Photoemission Spectroscopy*, Nat. Rev. Mater. **3**, 341 (2018).
- [10] B. Lv, T. Qian, and H. Ding, *Angle-Resolved Photoemission Spectroscopy and Its Application to Topological Materials*, Nat. Rev. Phys. **1**, 609 (2019).
- [11] J. A. Sobota, Y. He, and Z. X. Shen, *Angle-Resolved Photoemission Studies of Quantum Materials*, Rev. Mod. Phys. **93**, 1 (2021).
- [12] Z. Wang, A. Alexandradinata, R. J. Cava, and B. A. Bernevig, *Hourglass Fermions*, Nature **532**, 7598 (2016).
- [13] H. Watanabe, H. C. Po, M. P. Zaletel, and A. Vishwanath, *Filling-Enforced Gaplessness in Band Structures of the 230 Space Groups*, Phys. Rev. Lett. **117**, 096404 (2016).

- [14] S. Li, Y. Liu, S. S. Wang, Z. M. Yu, S. Guan, X. L. Sheng, Y. Yao, and S. A. Yang, *Nonsymmorphic-Symmetry-Protected Hourglass Dirac Loop, Nodal Line, and Dirac Point in Bulk and Monolayer X_3SiTe_6 ($X = Ta, Nb$)*, Phys. Rev. B **97**, 195109 (2018).
- [15] M. Rosmus, N. Olszowska, Z. Bukowski, P. Starowicz, P. Piekarczyk, and A. Ptok, *Electronic Band Structure and Surface States in Dirac Semimetal $LaAgSb_2$* , Materials (Basel). **15**, 7168 (2022).
- [16] S. Y. Yang, H. Yang, E. Derunova, S. S. P. Parkin, B. Yan, and M. N. Ali, *Symmetry Demanded Topological Nodal-Line Materials*, Adv. Phys. X **3**, 1414631 (2018).
- [17] T. Nakamura, S. Souma, Z. Wang, K. Yamauchi, D. Takane, H. Oinuma, K. Nakayama, K. Horiba, H. Kumigashira, T. Oguchi, T. Takahashi, Y. Ando, and T. Sato, *Evidence for Bulk Nodal Loops and Universality of Dirac-Node Arc Surface States in $ZrGeXc$ ($Xc=S, Se, Te$)*, Phys. Rev. B **99**, 245015 (2019).
- [18] A. Topp, J. M. Lippmann, A. Varykhalov, V. Duppel, B. V. Lotsch, C. R. Ast, and L. M. Schoop, *Non-Symmorphic Band Degeneracy at the Fermi Level in $ZrSiTe$* , New J. Phys. **18**, 125014 (2016).
- [19] L. M. Schoop, M. N. Ali, C. Straßer, A. Topp, A. Varykhalov, D. Marchenko, V. Duppel, S. S. P. Parkin, B. V. Lotsch, and C. R. Ast, *Dirac Cone Protected by Non-Symmorphic Symmetry and Three-Dimensional Dirac Line Node in $ZrSiS$* , Nat. Commun. **7**, 11696 (2016).
- [20] D. Takane, Z. Wang, S. Souma, K. Nakayama, C. X. Trang, T. Sato, T. Takahashi, and Y. Ando, *Dirac-Node Arc in the Topological Line-Node Semimetal $HfSiS$* , Phys. Rev. B **94**, 121108 (R) (2016).
- [21] C. Sims, M. M. Hosen, H. Aramberri, C. Y. Huang, G. Dhakal, K. Dimitri, F. Kabir, S. Regmi, X. Zhou, T. R. Chang, H. Lin, D. Kaczorowski, N. Kioussis, and M. Neupane, *Termination-Dependent Topological Surface States in Nodal-Loop Semimetal HfP_2* , Phys. Rev. Mater. **4**, 054201 (2020).
- [22] J. Bannies, E. Razzoli, M. Michiardi, H. H. Kung, I. S. Elfimov, M. Yao, A. Fedorov, J. Fink, C. Jozwiak, A. Bostwick, E. Rotenberg, A. Damascelli, and C. Felser, *Extremely Large Magnetoresistance from Electron-Hole Compensation in the Nodal-Loop Semimetal ZrP_2* , Phys. Rev. B **103**, 245104 (2021).
- [23] Z. Hao, W. Chen, Y. Wang, J. Li, X. M. Ma, Y. J. Hao, R. Lu, Z. Shen, Z. Jiang, W. Liu, Q. Jiang, Y. Yang, X. Lei, L. Wang, Y. Fu, L. Zhou, L. Huang, Z. Liu, M. Ye, D. Shen, J. Mei, H. He, C. Liu, K. Deng, C. Liu, Q. Liu, and C. Chen, *Multiple Dirac Nodal Lines in an In-Plane Anisotropic Semimetal*, Phys. Rev. B **104**, 115158 (2021).
- [24] H. Wu, A. M. Hallas, X. Cai, J. Huang, J. S. Oh, V. Loganathan, A. Weiland, G. T. McCandless, J. Y. Chan, S. K. Mo, D. Lu, M. Hashimoto, J. Denlinger, R. J. Birgeneau, A. H.

Nevidomskyy, G. Li, E. Morosan, and M. Yi, *Nonsymmorphic Symmetry-Protected Band Crossings in a Square-Net Metal PtPb₄*, *Npj Quantum Mater.* **7**, 31 (2022).

[25] N. Mohanta, J. M. Ok, J. Zhang, H. Miao, E. Dagotto, H. N. Lee, and S. Okamoto, *Semi-Dirac and Weyl Fermions in Transition Metal Oxides*, *Phys. Rev. B* **104**, 235121 (2021).

[26] W. Meng, Y. Liu, X. Zhang, Z. He, W. W. Yu, H. Zhang, L. Tian, and G. Liu, *Nonsymmorphic Symmetry Protected Spin-Orbit Semi-Dirac Fermions in Two Dimensions*, *Phys. Rev. B* **107**, 115167 (2023).

[27] G. Kresse and J. Hafner, *Ab Initio Molecular Dynamics for Liquid Metals*, *Phys. Rev. B* **47**, 558 (1993).

[28] G. Kresse and J. Hafner, *Ab Initio Molecular-Dynamics Simulation of the Liquid-Metamorphous-Semiconductor Transition in Germanium*, *Phys. Rev. B* **49**, 14251 (1994).

[29] G. Kresse and J. Furthmüller, *Efficiency of Ab-Initio Total Energy Calculations for Metals and Semiconductors Using a Plane-Wave Basis Set*, *Comput. Mater. Sci.* **6**, 50 (1996).

[30] G. Kresse and J. Furthmüller, *Efficient Iterative Schemes for Ab Initio Total-Energy Calculations Using a Plane-Wave Basis Set*, *Phys. Rev. B* **54**, 11169 (1996).

[31] P. E. Blöchl, *Projector Augmented-Wave Method*, *Phys. Rev. B* **50**, 17953 (1994).

[32] D. Joubert, *From Ultrasoft Pseudopotentials to the Projector Augmented-Wave Method*, *Phys. Rev. B - Condens. Matter Mater. Phys.* **59**, 1758 (1999).

[33] J. P. Perdew, K. Burke, and M. Ernzerhof, *Generalized Gradient Approximation Made Simple*, *Phys. Rev. Lett.* **77**, 3865 (1996).

[34] <http://www.xcrysden.org/>

[35] G. Pizzi, V. Vitale, R. Arita, S. Blügel, F. Freimuth, G. Géranton, M. Gibertini, D. Gresch, C. Johnson, T. Koretsune, J. Ibañeta-Azpiroz, H. Lee, J. M. Lihm, D. Marchand, A. Marrazzo, Y. Mokrousov, J. I. Mustafa, Y. Nohara, Y. Nomura, L. Paulatto, S. Poncé, T. Ponweiser, J. Qiao, F. Thöle, S. S. Tsirkin, M. Wierzbowska, N. Marzari, D. Vanderbilt, I. Souza, A. A. Mostofi, and J. R. Yates, *Wannier90 as a Community Code: New Features and Applications*, *J. Phys. Condens. Matter* **32**, 165902 (2020).

[36] Q. S. Wu, S. N. Zhang, H. F. Song, M. Troyer, and A. A. Soluyanov, *Wannier Tools: An Open-Source Software Package for Novel Topological Materials*, *Comput. Phys. Commun.* **224**, 405 (2018).

[37] P. E. R. Blanchard, R. G. Cavell, and A. Mar, *On the Existence of ZrAs₂ and Ternary Extension Zr(Ge_xAs_{1-x})As (0 ≤ x ≤ 0.4)*, *J. Alloys Compd.* **505**, 17 (2010).

[38] S. Nandi, B. B. Maity, V. Sharma, R. Verma, V. Saini, B. Singh, D. Aoki, and A. Thamizhavel, *Magnetotransport and Fermi Surface Studies of a Purported Nodal Line Semimetal ZrAs₂*, Phys. Rev. B **109**, 075155 (2024).

Figures

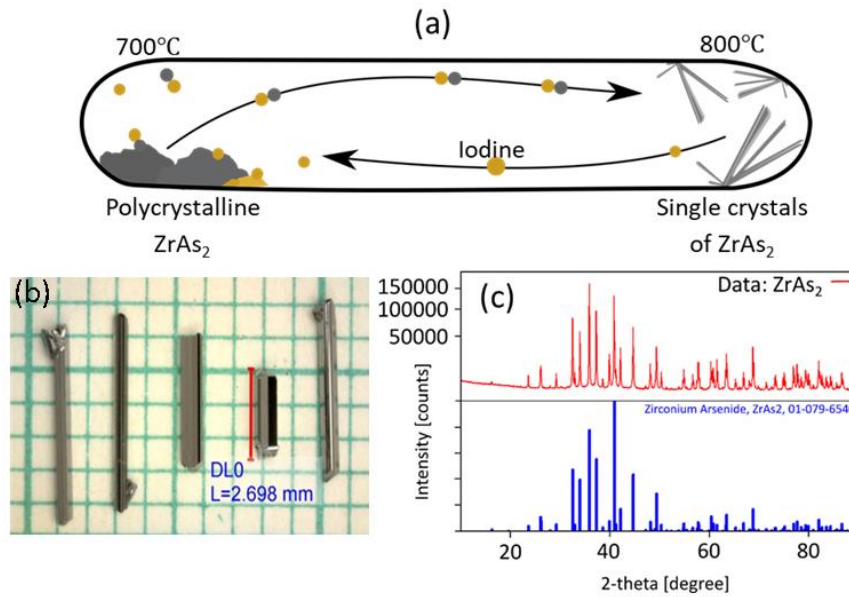


Figure 1: (a) Schematic of the chemical vapor transport for ZrAs_2 synthesis, with source zone at 700 °C and growth zone at 800 °C, (b) needle-like ZrAs_2 single crystals obtained through the process and (c) powder X-ray diffraction of the crystals.

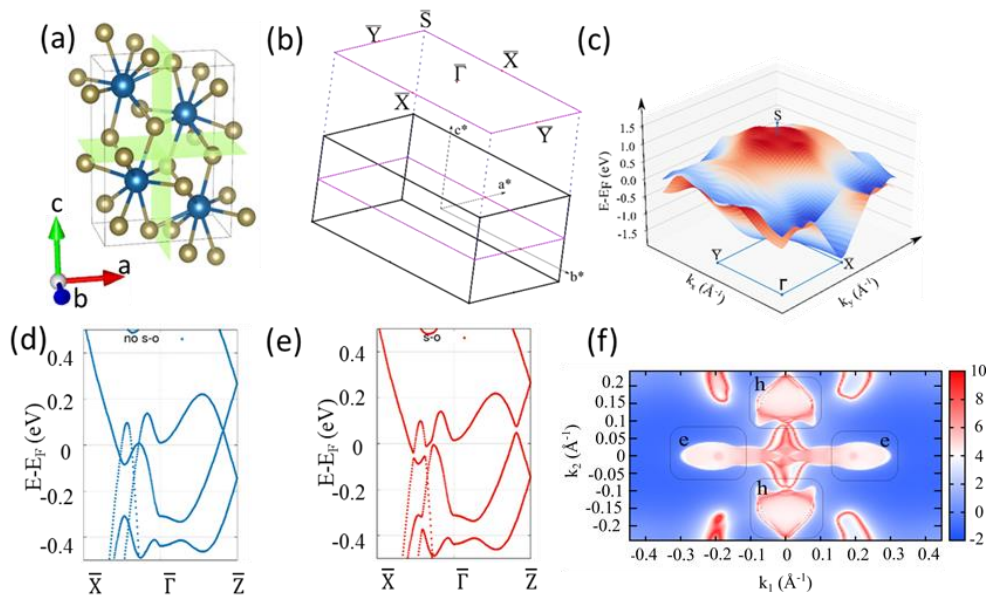


Figure 2: (a) Crystal structure of ZrAs_2 showing non-symmorphic symmetry, (b) 3D Brillouin zone and projection on (001) plane with high symmetry points, (c) 3D visualization of the bands with SOC, band structure along $\bar{X}-\bar{\Gamma}-\bar{Z}$ high symmetry path (d) without SOC, (e) with SOC, and (f) theoretically calculated Fermi surface with $\bar{\Gamma}$ at the center presenting electron (e) and hole (h) pockets.

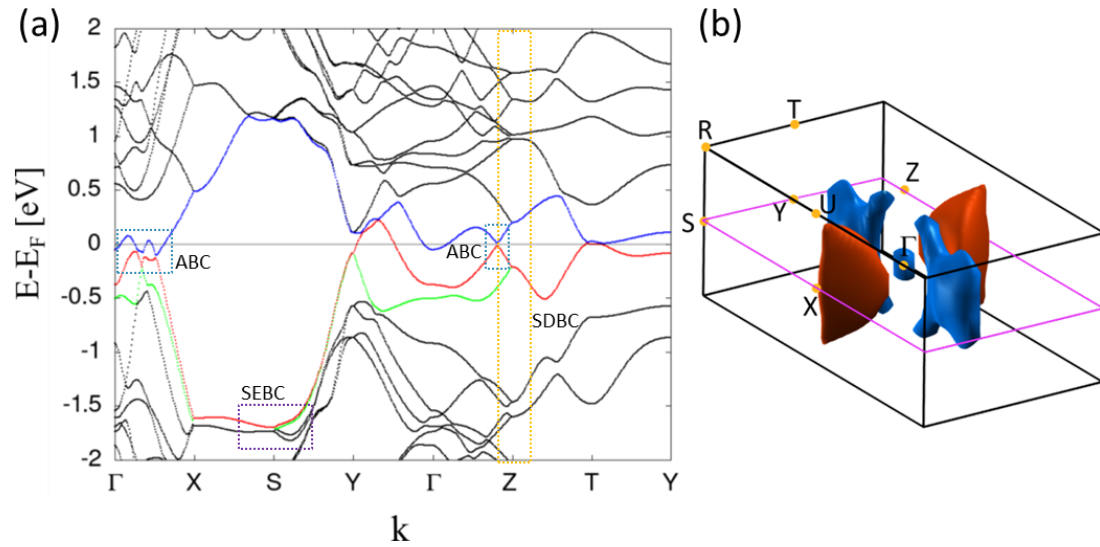


Figure 3: (a) Theoretical band structure with SOC showing band contributing to electron pocket (blue color), red and green color bands contributing hole-type pockets and (b) 3D Brillouin zone of ZrAs_2 showing electron pocket (blue) and hole pocket (red).
 *SDBC: Semi Dirac band crossings (yellow), ABC: accidental band crossings (teal), SEBC: symmetry enforced band crossings (purple)

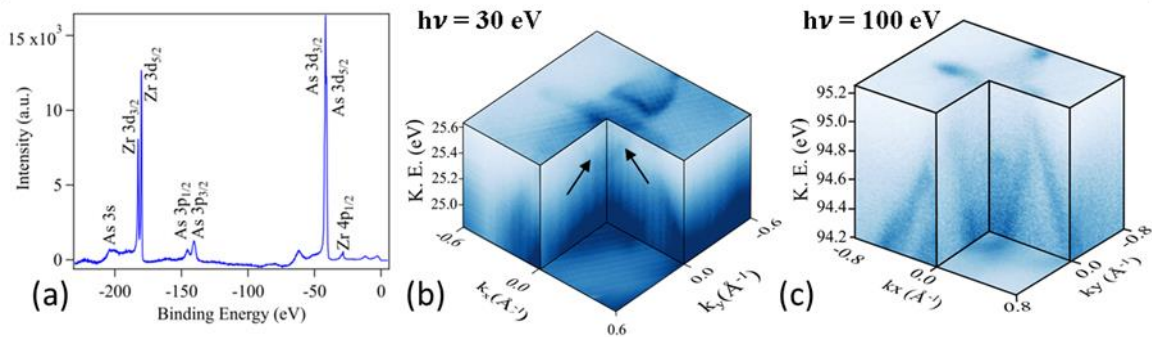


Figure 4: (a) core-level spectra of ZrAs_2 indicating Zr and As peaks confirming the only elements in ZrAs_2 , 3D visualization of ARPES data for ZrAs_2 obtained at excitation energy: (b) 30 eV and (c) 100 eV.

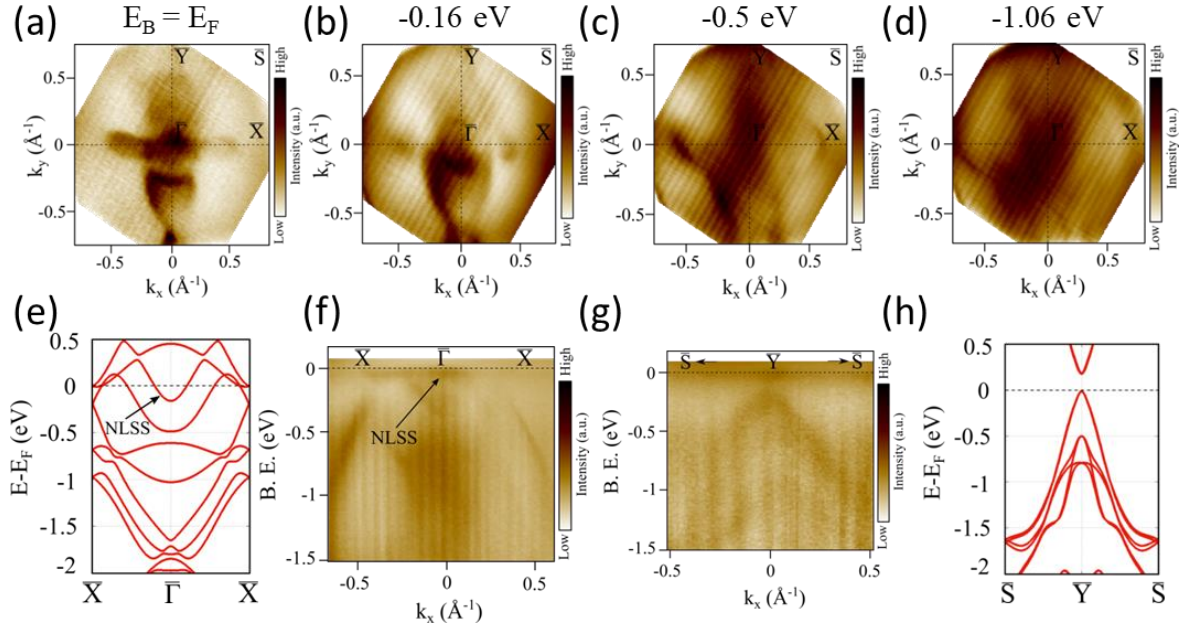


Figure 5: The constant energy contour of ZrAs_2 taken at 30 eV at binding energies equal to: (a) E_F , (b) -0.16 eV, (c) -0.5 eV, (d) -1.06 eV, theoretically calculated band structure along (e) $\bar{X}\bar{\Gamma}\bar{X}$, (h) $\bar{S}\bar{Y}\bar{S}$ and experimentally obtained band structure along (f) $\bar{X}\bar{\Gamma}\bar{X}$ (h) $\bar{S}\bar{Y}\bar{S}$.

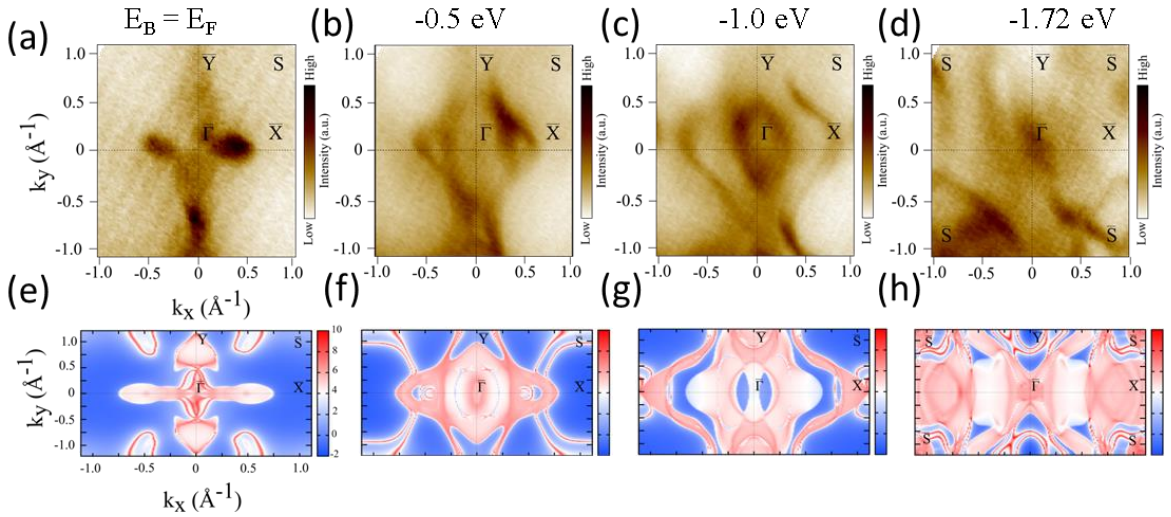


Figure 6: Comparison between constant energy contours obtained by ARPES and DFT calculations at binding energy equal to: (a, e) E_F , (b, f) -0.5 eV, (c, g) -1.0 eV and (d, h) -1.72 eV.

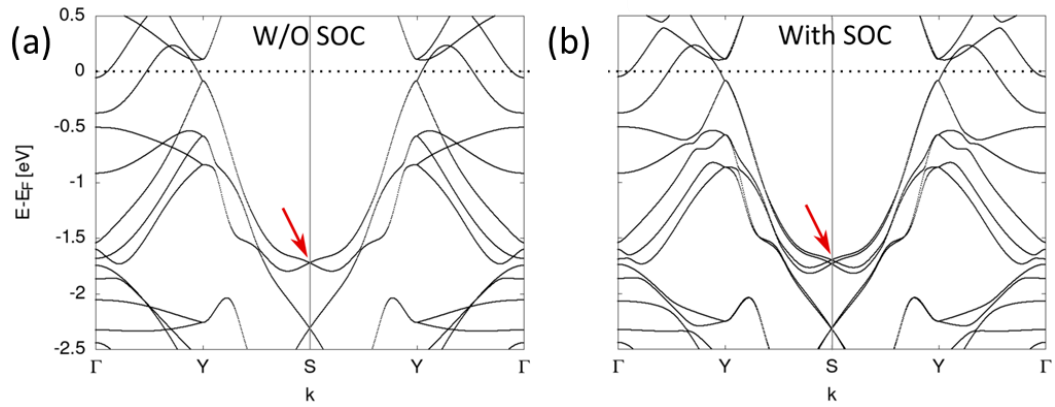


Figure 7: Bulk band dispersion: (a) without SOC and (b) with SOC along $\bar{\Gamma}-\bar{Y}-\bar{S}-\bar{Y}-\bar{\Gamma}$ showing Dirac band crossing (red arrow) at \bar{S} point (-1.72 eV).

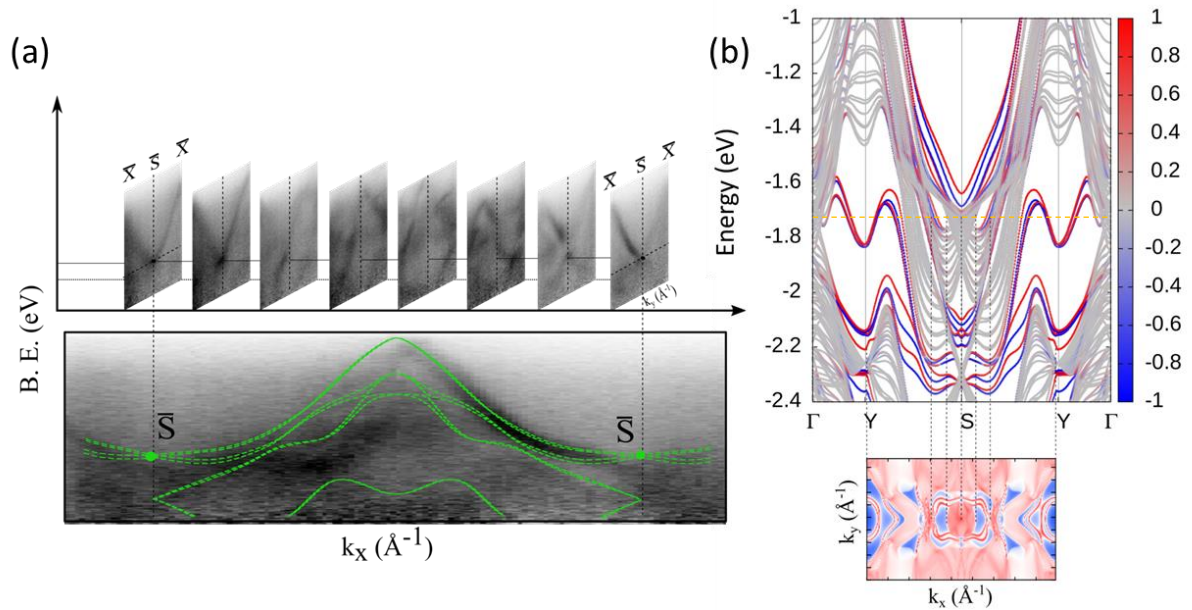


Figure 8: (a) Overlay of bands calculated via DFT (green color dotted lines) with those obtained experimentally by ARPES, showcasing possible Dirac-like crossings at the \bar{S} points. Additionally, it contains multiple slices taken along the $\bar{X}-\bar{S}-\bar{X}$ direction to exhibit the evolution of bands across the $\bar{S}-\bar{Y}-\bar{S}$ vector and (b) shows the slab calculations with projection of bands on iso-energetic surface calculated at -1.72 eV.

Supplemental Material

Emergent impervious band crossing in the bulk in topological nodal line semimetal ZrAs_2

A. S. Wadge^{1*}, K. Zborecki^{3†}, B. J. Kowalski², D. Jastrzebski^{1,2,5}, P. K. Tanwar¹, P. Iwanowski², R. Diduszko², A. Moosarikandy¹, M. Rosmus⁴, N. Olszowska⁴ and A. Wisniewski^{1,2}

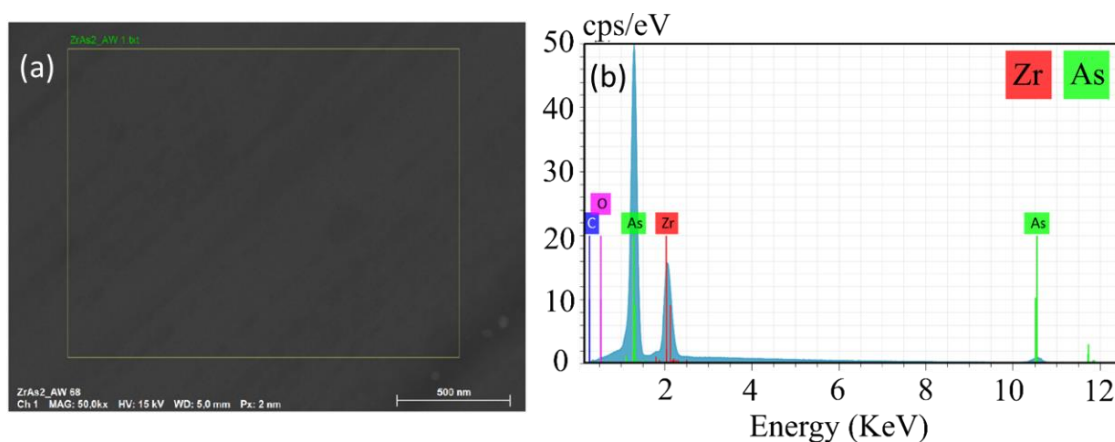
¹International Research Centre MagTop, Institute of Physics, Polish Academy of Sciences, Aleja Lotnikow 32/46, PL-02668 Warsaw, Poland

²Institute of Physics, Polish Academy of Sciences, Aleja Lotnikow 32/46, PL-02668 Warsaw, Poland

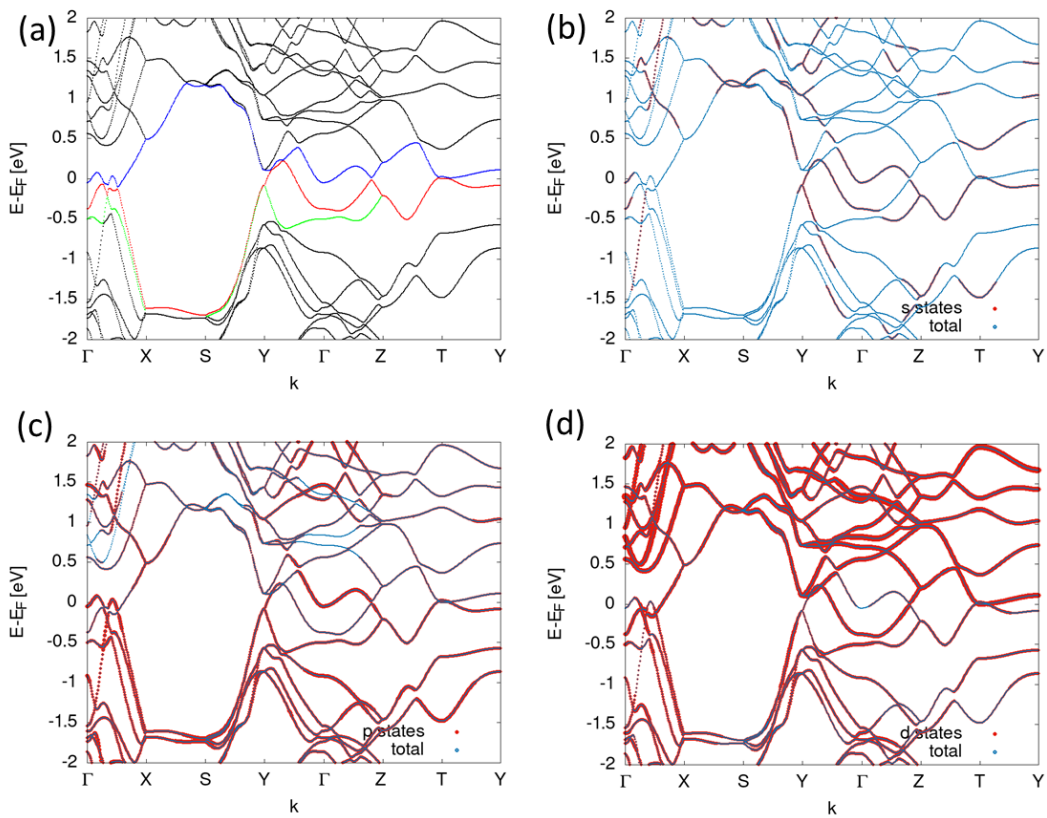
³Faculty of Physics, Warsaw University of Technology, Koszykowa 75, Warsaw, 00-662, Poland

⁴National Synchrotron Radiation Centre SOLARIS, Jagiellonian University, Czerwone Maki 98, PL-30392 Cracow, Poland

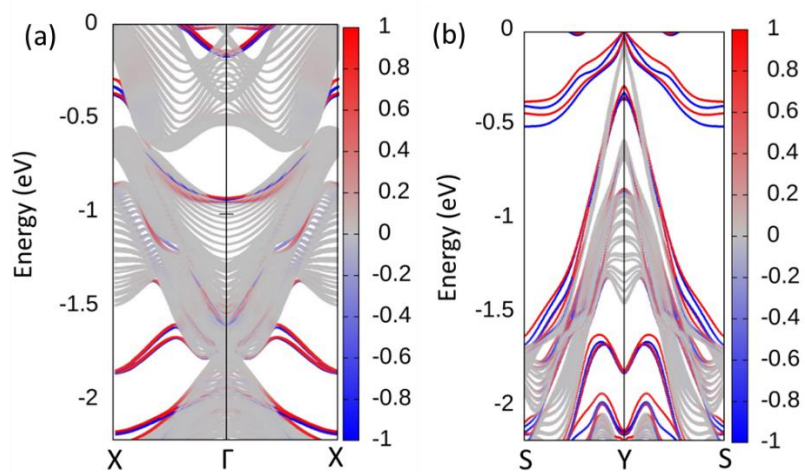
⁵Faculty of Chemistry, Warsaw University of Technology, Noakowskiego 3, 00-664 Warsaw, Poland



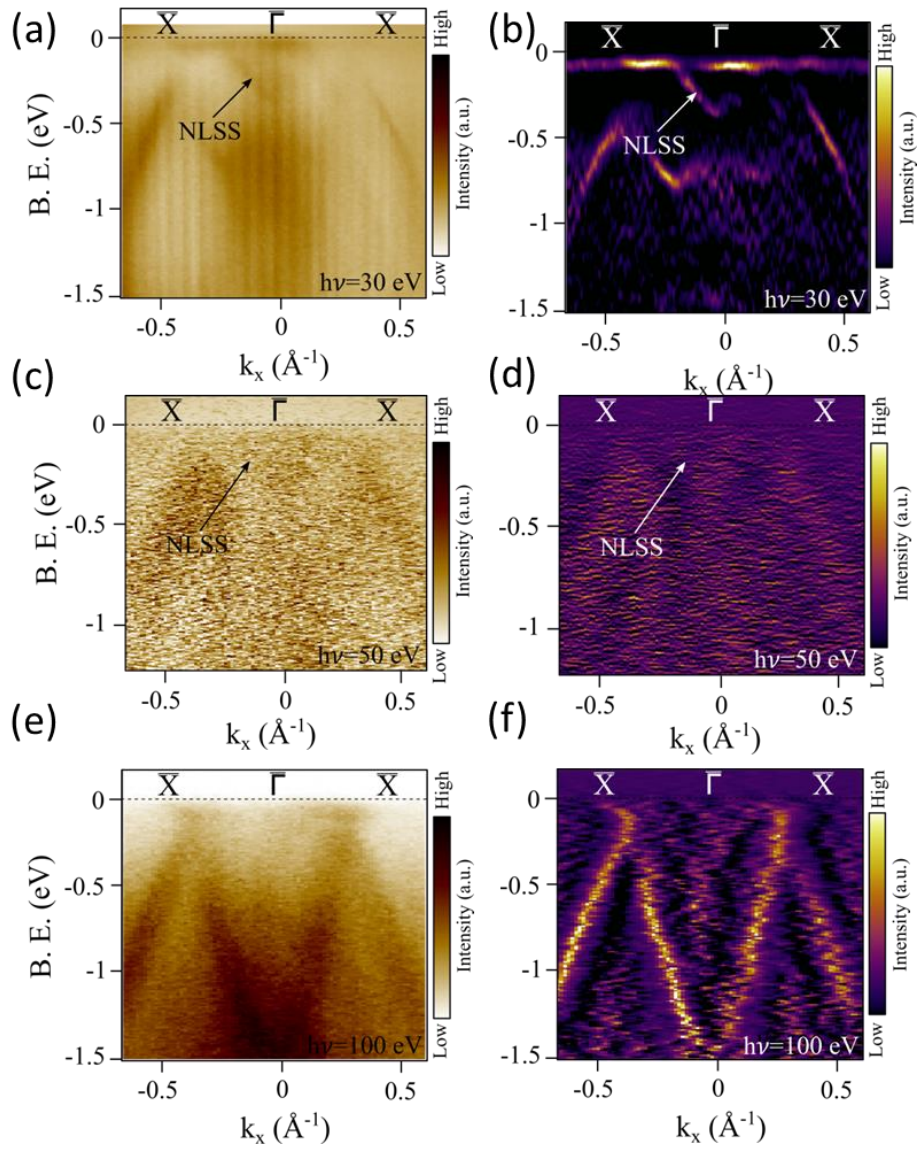
Suppl. Figure.1: (a) SEM image of the surface of ZrAs_2 , (b) EDX spectrum taken on the shown surface presenting significant Zr and As peaks.



Suppl. Figure.2: Total bulk band structure and orbital contributions of ZrAs_2 : (a) total bulk band structure displaying the overall electronic states, contribution of (b) s orbital states, (c) p orbital states and (d) d orbital states to the total band structure.

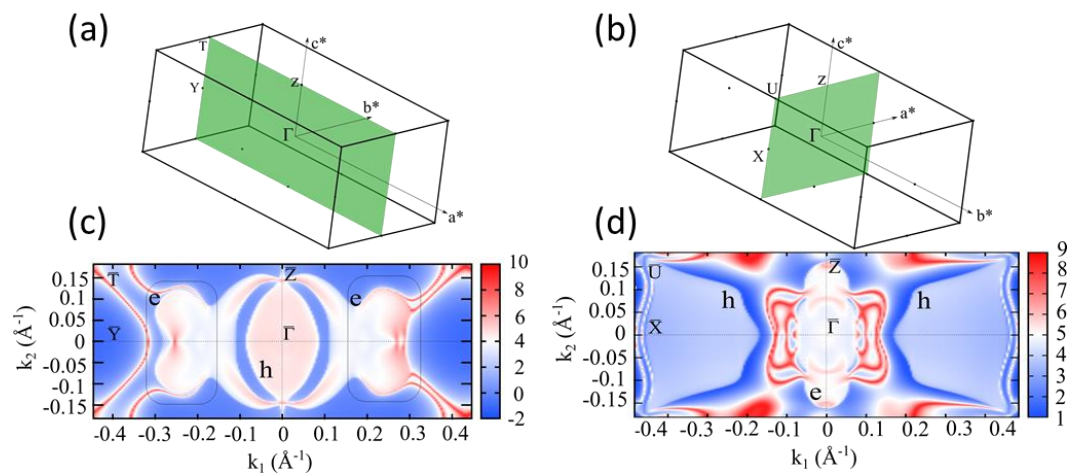


Suppl. Figure 3: the slab calculations: (a) taken along the $\bar{X}\bar{\Gamma}\bar{X}$ and (b) $\bar{S}\bar{Y}\bar{S}$.



Suppl. Figure 4. Experimentally obtained band dispersion and corresponding 2D curvature along $\bar{X}\bar{\Gamma}\bar{X}$ at excitation energies (a, b) 30 eV, (c, d) 50 eV and (e, f) 100 eV, respectively.

*NLSS: Nodal line surface states



Suppl. Figure 5 Brillouin zone showing plane along (a) (100) , (b) (010) indicated by green color with theoretically calculated Fermi surface ($E = E_F$) with $\bar{\Gamma}$ at the center on (c) (100) and (d) (010) plane indicating electron (e) and hole (h) pockets.